Resolution of well-known resistivity equivalences by inclusion of time-domain induced polarization data

Short title: Comparison of DC and DCIP

Authors:

Line Meldgaard Madsen*, linemeldaard@geo.au.dk

Gianluca Fiandaca*, gianluca.fiandaca@geo.au.dk

Anders Vest Christiansen*, anders.vest@geo.au.dk

Esben Auken*, esben.auken@geo.au.dk

*HydroGeophysics Group, Department of Geoscience, Aarhus University
C. F. Møllers Allé 4, DK-8000 Aarhus C, Denmark

Day of submission: 05.01.17

Day of resubmission: 23.05.2017

Accepted: October 2017

Key words: Electrical/resistivity; Induced polarization; Inversion;

ABSTRACT

The principle of equivalence is known to cause non-uniqueness in interpretations of direct-current (DC) resistivity data. Low or high-resistivity equivalences arise when a thin geological layer with a low/high resistivity is embedded in a relative high/low resistivity background formation causing strong resistivity-thickness correlations. The equivalences often make it impossible to resolve embedded layers. Here, we show that the equivalence problem can be significantly reduced by combining the DC data with full-decay time-domain induced polarization (IP) measurements. We apply a 1D Markov Chain Monte Carlo algorithm to invert synthetic DC resistivity data of models with low and high-resistivity equivalences. By applying this inversion method, it is possible to study the space of equivalent models, which have an acceptable fit to the observed data, and to make a full sensitivity analysis of the model parameters. We then include a contrast in chargeability into the model, modelled in terms of spectral Cole-Cole IP parameters, and invert the DC and IP data in combination. The results show that the addition of IP data largely resolves the DC equivalences. Furthermore, we present a field example where DC and IP data are measured on a sand formation with an embedded clay layer known from a borehole drilling. Inversion results show that the DC data alone do not resolve the clay layer due to equivalence problems, but by adding the IP data to the inversion, the layer is resolved.

INTRODUCTION

The DC resistivity method, also known as the geoelectrical resistivity method, is one of the most used methods for mapping the electrical resistivity of subsurface geological layers. The method has well-known inherent ambiguities related to the principle of equivalence and equivalent layer sequences are investigated in several text books and papers (e.g. Koefoed, 1979, Knödel et al., 2007). Best known are the low- and high-resistivity equivalences (also referred to as S- and T-type equivalences), which arise when a thin layer with a relative low/high resistivity is present in a background formation with a high/low resistivity. For these equivalences, it is impossible to determine a unique solution for the model parameters, resistivity and layer thickness, of the thin layer. However, due to the correlation between the parameters, the thickness-resistivity ratio (the conductance) is well-determined for low-resistivity equivalences and the thickness-resistivity product (the resistance) is well-determined for high-resistivity equivalences (Fitterman et al., 1988).

A way to resolve equivalences and to improve model resolution is by using complementary geophysical methods. Several field surveys and quantitative analyses have been carried out with combined or joint inversion of two or more different data sets from the same location (e.g. Vozoff and Jupp, 1975, Raiche et al., 1985, Seara and Granda, 1987, Sandberg, 1993, Christiansen et al., 2007). Raiche et al. (1985) showed that a significant improvement in resolution of layered-earth models can be obtained by applying a joint inversion of transient electromagnetic data (TEM) and DC data compared to results obtained with either TEM or DC data alone. Sandberg (1993) showed that adding induced polarization (IP) data to a joint inversion of TEM and DC improves the resolution further.

If the subsurface is chargeable when acquiring DC data, the DC response will be accompanied by the IP effect, which manifests itself as a slow rise and decay of the potential after the injected current is turned on and off. Consequently, by measuring the time-varying potential at the current turn on/off, the IP effect can be measured in combination with the DC data (e.g. Binley and Kemna, 2005) in the time-domain (TD). The spectral content of the IP phenomenon can be extracted from the TDIP transients, and often the Cole-Cole model (Cole and Cole, 1941, Pelton et al., 1978) is used to model the IP effect in the inversion of the TDIP data (e.g. Hönig and Tezkan, 2007, Fiandaca et al., 2012, 2013). Outside mineral exploration, the combined DCIP method is frequently applied for lithology discrimination and characterization (e.g. Gazoty et al., 2012b, Chongo et al., 2015, Johansson et al., 2016, Maurya et al., 2016) as well as investigations of contaminated sites (e.g. Aristodemou and Thomas-Betts, 2000, Sogade et al., 2006, Leroux et al., 2007, Gazoty et al., 2012a, Johansson et al., 2015).

The aim of this study is to show that the application of spectral information retrieved from TDIP data helps to reduce the well-known resistivity-thickness equivalences seen with DC resistivity models and therefore increases the reliability of inversion results dramatically with only little effort. We show this by using a Markov Chain Monte Carlo (MCMC) inversion method to invert DC data alone and then DC and TDIP data in combination. This allows us to study the space of equivalent models in detail. The MCMC method also allows for studies of parameter correlations and the full sensitivities of the nonlinear problem, which is essential when studying equivalences. In the following, we investigate synthetic examples of low- and high-resistivity equivalences and show that thickness-resistivity equivalences observed with DC data alone can be resolved by adding TDIP data where a layer contrast exist in just one of the Cole-Cole IP parameters. Finally, we present a field

example where the IP data help to resolve a clay layer (known from boreholes) embedded in a sand formation.

METHODOLOGY

Data space

When inverting TD DCIP data, the data space is composed by the apparent resistivity values, ρ_a, and full-decay chargeability, M, which are computed from the transient IP decay as described by Gazoty et al. (2012b). A log-transform is applied to enhance linearity, so the data vector, $\boldsymbol{d_{obs}}$, is given as

$$\boldsymbol{d_{obs}} = \{\log(\rho_{a,q}), \log(M_{q,g})\}$$

$$q = 1{:}\,N_{quadrupoles};\ g = 1{:}\,N_{gates}, \quad (1)$$

where $\rho_{a,q}$ is the apparent resistivity measured at quadrupole q and $M_{q,g}$ is the chargeability of the g^{th} time gate of the IP decay recorded at quadrupole q. In the case of negative chargeability data, the inversion is carried out in the linear space without the log-transform.

The analyses in this study are based on data simulated over a 1D Earth as a vertical sounding with 20 quadrupoles with current electrode spacing, |AB|, from 7.5 m to 500 m and potential electrode spacing, |MN|, from 2.5 m to 65 m (Table 1). With these electrode configurations, the geometric factor is limited to 3000 m in order to keep a good signal-to-noise ratio (Gazoty et al., 2013).

The applied waveform has a 100% duty cycle as described by Olsson et al. (2015), where the data measurements are performed in the current-on time. Compared to the traditional

50% duty cycle waveform, where the current is switched off before measurements are made, the 100% duty cycle reduces the acquisition time to half and increases the signal-to-noise ratio due to signal superposition. The synthetic IP decays are simulated from 2.5 ms to 10,000 ms after the current switch. The signal is then divided into 35 time gates with logarithmically increasing gate lengths from 0.8 ms to 2040 ms.

Gaussian noise is added to the data to simulate the noise level in the field (Gazoty et al., 2013). The applied noise model is described in Olsson et al. (2015), where a total standard deviation, STD_{total}, is computed by summing a squared uniform term, STD_{uni}, and a voltage-dependent term, STD_{vth}, for each data point or time gate g:

$$STD_{total}^2(g) = STD_{uni}^2(g) + STD_{vht}^2(g) \tag{2}$$

where STD_{vht} is the effect of the signal level on the data uncertainty computed as

$$STD_{vht}(g) = \frac{V_{TH}}{V_{IP}(g)} \frac{\sqrt{D_{nom}}}{D(g)} \frac{1}{\sqrt{N_{stacks}}} \tag{3}$$

where $V_{IP}(g)$ is the measured voltage level, $D(g)$ is the gate width, and N_{stacks} is the number of stacked pulses. D_{norm} is the nominal gate width for a voltage noise threshold value, V_{TH}. In practice, data points that fall below the voltage threshold will be given a larger standard deviation. In this study, a $STD_{uni} = 2\%$ has been used for DC data and a $STD_{uni} = 5\%$ has been used for IP data with $V_{TH} = 0.1\, mV$ for $D_{norm} = 0.01\, s$. Three stacks have been considered for each quadrupole measurement.

Model space and forward modeling

Using the Cole-Cole model for parameterization, the complex resistivity is given as a function of frequency (Pelton et al., 1978):

$$\zeta_n(\omega) = \rho_n \left[1 - m_{0_n}\left(1 - \frac{1}{1 + (i\omega\tau_n)^{c_n}}\right)\right] \tag{4}$$

where for the n^{th} layer, ρ is the resistivity and m_0, τ, and c are the IP parameters. Adding the layer thicknesses, thk, the model vector, $\boldsymbol{m}$ adds up to:

$$\boldsymbol{m} = \left\{\log(\rho_n), \log\left(m_{0_n}\right), \log(\tau_n), \log(c_n), \log(thk_m)\right\}$$

$$n = 1{:}\,N_{layers};\ m = 1{:}\,N_{layers} - 1 \tag{5}$$

Given a layered-earth model, the algorithm presented in Fiandaca et al. (2012) is used to model the TDIP forward response. This algorithm applies the full-decay waveform and models the transmitter current waveform and the receiver transfer function accurately.

Linearized inversion and uncertainties

A linearized inversion approach is used to determine the start model for the MCMC inversion algorithm described in the next section. The linearized inversion of 1D DC data follows the algorithm described in Auken et al. (2005). The algorithm was later extended to include IP data as well (Fiandaca et al., 2012). In these inversion approaches, the uncertainty analyses of the model parameters are computed through the posterior covariance of the linear mapping, C_{est}, as described by Tarantola and Valette (1982a). Due to the logarithmic transform applied in the inversion, the uncertainty on the model parameter m_i is given as a standard deviation factor (STDF) defined as

(6)

$$STDF(m_i) = \exp\left(\sqrt{C_{est(i,i)}}\right)$$

where the 68% confidence interval for m_i is between

$$\frac{m_i}{STDF(m_i)} < m_i < m_i \cdot STDF(m_i). \quad (7)$$

A perfect resolution will give a STDF = 1 and using the terminology from Auken et al. (2005) a STDF < 1.2 indicates a well-resolved parameter, 1.2 < STDF < 1.5 indicates a moderately resolved parameter, 1.5 < STDF < 2 indicates a poorly resolved parameter, and STDF > 2 indicates an unresolved parameter.

MCMC inversion

Following a probabilistic formulation, the posterior probability distribution of the model $\boldsymbol{m}$ is given as (Tarantola, 2005)

$$P_{post}(\boldsymbol{m}) = K\, P_{prior}(\boldsymbol{m})\, P_{like}(\boldsymbol{m}) \quad (8)$$

where $P_{prior}(\boldsymbol{m})$ is the prior probability distribution given by prior information, $P_{like}(\boldsymbol{m})$ is the likelihood function describing the degree of fit between the observed data and the forward response of the model $\boldsymbol{m}$, and K is a normalization constant. The objective of the inversion is to describe the posterior probability distribution and thereby determine the space of models with the highest probability. Assuming the uncertainties of the model parameters to be Gaussian, the likelihood can be written (Mosegaard and Tarantola, 2002):

$$P_{like} = k \cdot \exp\left[-\frac{1}{2}\left(\boldsymbol{g}(\boldsymbol{m}) - \boldsymbol{d_{obs}}\right)^T \boldsymbol{C_{obs}}^{-1}\left(\boldsymbol{g}(\boldsymbol{m}) - \boldsymbol{d_{obs}}\right)\right] \quad (9)$$

where $\boldsymbol{d_{obs}}$ holds the observed data, $\boldsymbol{g(m)}$ is the forward response of $\boldsymbol{m}$, $\boldsymbol{C_{obs}}$ is the covariance matrix of the observed data, and k is a normalization constant. If needed, the likelihood function can easily be extended in order to contain regulations terms as well.

MCMC methods have previously been applied to geophysical inversion problems to describe the posterior probability distribution (Tarantola and Valette, 1982b, Mosegaard and Tarantola, 1995, Mosegaard and Tarantola, 2002). In this study, the method is applied with a Metropolis-Hastings sampling algorithm (Metropolis et al., 1953, Hastings, 1970), where a random walk samples models directly from the posterior probability distribution. The sampling algorithm repeats two steps. Firstly, a new model, $\boldsymbol{m_{new}}$, is proposed. The new model is then accepted or rejected based on the likelihood ratio between $\boldsymbol{m_{new}}$ and the last accepted model, here referred to as the current model, $\boldsymbol{m_{cur}}$. In this way, a Markov chain of models is sampled, where $\boldsymbol{m_j}$ is dependent only on $\boldsymbol{m_{j-1}}$ and none of the previous models (the Markov property). The algorithm will sample models with high probability more frequently and thereby converge towards the posterior probability distribution.

The MCMC algorithm applied for inversion of DCIP data is presented as a pseudo-algorithm in Table 2. Before the routine is started, the variables N_{ite} and k_{step} are initialized (Step 1). These are the number of iterations and a step length constant, which is later used to define the model perturbation for the MCMC sampling. A linearized inversion is then performed to determine the start model for the MCMC model sampling (Step 2). This is done to minimize the burn-in phase of the MCMC algorithm, thereby reducing the inversion time. Hereafter the MCMC sampling (Step 4 - Step 13) is started using a scaled model proposer (Step 5) to compute the next model, $\boldsymbol{m_{new}}$, in a random walk:

$$\boldsymbol{m_{new}} = \boldsymbol{m_{cur}} + \boldsymbol{L}\,\boldsymbol{n}\,k_{step} \tag{10}$$

where k_{step} is the predefined step length constant, $\boldsymbol{n}$ is a vector of random numbers drawn from a Gaussian distribution, and $\boldsymbol{L}$ is the Cholesky decomposition of $\boldsymbol{C_{est}}(\boldsymbol{m_{start}})$, so

$$\boldsymbol{C_{est}}(\boldsymbol{m_{start}}) = \boldsymbol{L}\boldsymbol{L}^T \tag{11}$$

The Cholesky decomposition of the matrix is applied to the model perturbation to scale the step length between the current model and the proposed new model. By scaling the model proposer with $\boldsymbol{C_{est}}$, the different interval ranges and the uncertainty of the individual Cole-Cole parameters are taken into account. The scaling lets the algorithm take larger steps for parameters with a high uncertainty and therefore leads to a faster convergence. It was found that by applying the scaled model proposer, the algorithm converges over 200 times faster compared to a standard Gaussian proposer (Madsen et al., 2016). For a homogenous half-space, this means that the number of iterations necessary to reach convergence is brought down from 1,000,000 to 5000 models. Running on ten CPUs, this is a decrease in the inversion time from approximately one day to ten minutes.

The acceptance probability, P_{acc}, of the proposed model is computed as the likelihood ratio (Step 6) as given by Mosegaard and Tarantola (1995). When computing the ratio, the normalization constant from the likelihood equation (Eq. 9) cancels out because it is present in both the numerator and the denominator. If the likelihood of the new model is higher than the likelihood of the current model, the new model will always be accepted to the Markov chain and will become the new $\boldsymbol{m_{cur}}$. If, however, the likelihood of the new model is lower than the likelihood of the current model, the new model will only be accepted with probability P_{acc} as outlined in Step 7-12.

The uncertainty of the model parameters is computed as the standard deviation from the mean of each marginal posterior probability distribution. The uncertainties are then

expressed as STDFs as for the linearized approach. The variation of the standard deviation during the sampling is used to check the convergence. When the standard deviations of the marginal posterior probability distributions have converged, the probability distribution has converged as well and the number of iterations has been sufficient.

RESULTS

Low and high-resistivity equivalences

A low-resistivity equivalence (S-type equivalence) arises when a thin layer with a relatively low resistivity is embedded in a formation with a higher resistivity. The thickness and the resistivity of the embedded layer cannot be resolved whereas the conductance is fairly well-determined.

The apparent resistivity data in Figure 1 is the synthetic forward response of a three-layer model, which has a low-resistivity layer embedded in a high-resistivity formation where the resistivity values are ρ = [200, 20, 200] Ωm and the associated thicknesses are thk = [10, 5] m. These DC data are inverted with the MCMC algorithm with 200,000 iterations and the result is presented in Figure 2 (Panel-DC). Here, the density of the black lines illustrates the density of accepted models and is therefore an image of the posterior probability distribution. The model found to have the highest probability (yellow dashed line) is not consistent with the true model (red line) in the low resistivity layer. The STDFs of the model parameters found from the MCMC inversion results are listed in Table 3 (Row 1). The STDFs show that the parameters of the top and bottom layer are well-resolved by the inversion scheme, but the probability distributions of the thickness and the resistivity of the embedded low-resistivity layer do not converge and the parameters can not be determined.

The models accepted by the MCMC algorithm spans the space of equivalent models. There is a clear negative correlation between the resistivity and the thickness of the embedded layer (Figure 2, Panel-DC). In the second layer, as the resistivity of the equivalent models decreases the thickness decreases as well keeping the conductance constant. The STDF of the conductance is 1.04, which indicates a well-resolved parameter.

A number of other low-resistivity models with varying layer thicknesses have been inverted with the MCMC algorithm to study the respective equivalences. With the resistivity contrast presented in Figure 2 (Panel-DC), strong equivalences causing unresolved parameters are found to be present until the embedded layer is given a thickness, which is three times the thickness of the top layer.

To study the influence of TDIP data on the resistivity-thickness equivalences, TDIP data are added to the existing DC data and a joint inversion performed in terms of Cole-Cole parameters. The true model is plotted together with the MCMC inversion result in Figure 2 (Panel-DCIP) for all three IP parameters. The time constant, τ, and the frequency exponent, c, take the same values in all three layers and only a contrast is present in the model space chargeability, m_0, where the embedded layer has a relatively high chargeability ($m_0 = [20, 200, 20]\ mV/V$). The synthetic TDIP data are shown in Figure 3.

The inversion result of the joint DCIP data shows that adding IP data to the inversion helps resolving the thickness of the embedded layer and therefore decreases the amount of equivalent models. The thickness and the resistivity are still negatively correlated, but because the space of equivalent models is reduced, both the resistivity and the thickness of the second layer are now well-resolved with a STDF < 1.2 (Table 3, Row 2).

The degree to which the equivalences are resolved depends on the magnitude of the contrast in chargeability between the layers. In Figure 2 (Panel-DCIP), the chargeability contrast has the same magnitude as the contrast in the resistivity, i.e. a factor of ten, which gives us a realistic model for field measurements of a clay layer embedded in a sand formation. If this contrast is reduced, the resolution of the model will decrease. MCMC analyses of models with different chargeability contrasts indicate that as long as the contrast is more than a factor of six (i.e. m_0 = [20, 120, 20] mV/V), the MCMC maximum probability model corresponds to the true model and the model parameters are resolved.

The influence of IP has also been studied in models with high-resistivity equivalences (T-type equivalence), where a high-resistivity layer is embedded in a low-resistivity formation (Figure 4). The high-resistivity equivalences in the DC inversion results (Figure 4, Panel-DC) are similar and of the same magnitude as those observed for models with low-resistivity equivalences. IP data with a chargeability contrast between the layers were added to the inversion and the DCIP data inverted together (Figure 4, Panel-DCIP). The high-resistivity equivalences are resolved with a contrast in the chargeability similar to the low-resistivity case, i.e. a factor of six.

If contrasts are given to any of the other IP parameters in an inversion, the equivalences are reduced as well. When the lithology changes between layers, not only do the resistivity and the chargeability change, but the value of the time constant, τ, and the frequency exponent, c, will usually change as well. Therefore, if a contrast is added in τ or c then the contrast in the chargeability can be much less than a factor of ten and the equivalences will still be resolved. An example of this is shown later with field data.

Equivalences and parameter contrasts

To study possible equivalences in IP data and to determine to what extent IP parameter contrasts between layers can resolve layer thicknesses, a three-layer DCIP model is constructed with no contrast between the layers, i.e. reassembling a homogenous half space. This default model is given the Cole-Cole parameters: $\rho = 200\,\Omega m$, $m_0 = 100\,mV/V$, $\tau = 1\,s$, $c = 0.6$. The thickness of layer one and two are 10 m and 5 m, respectively. For one Cole-Cole parameter at a time, the parameter value of the embedded layer is then changed and a MCMC inversion performed in order to study how well this single parameter contrast is able to resolve the thickness of the layers. The resulting uncertainty analysis of the thickness of the embedded layer is shown in Figure 5. If the STDFs computed over the marginal posterior probability distributions are above 2.5, the STDF in the figure is set to 2.5 indicating an unresolved parameter.

The blue line in Figure 5 represents a number of models where the resistivity of the second layer varies between 20 Ωm and 2000 Ωm in a background formation of 200 Ωm. We see that no matter the resistivity contrast, low-resistivity and high-resistivity equivalences are present making it impossible to resolve the thickness of the embedded layer. When changing the chargeability of the embedded layer (Figure 5, red line), the increase in resolution of the layer is larger for a decreasing relative chargeability compared to an increasing value. So, for the case studied here, it is easier to resolve the layer thickness of an embedded low chargeable layer than from a high chargeable layer. For a contrast between the layers in c, only a factor of one half, e.g. c = [0.6, 0.3, 0.6], is required to gain a well-resolved layer thickness (Figure 5, purple line). For a contrast in τ (Figure 5, yellow line), it is only possible to resolve the layer thickness moderately. τ is the Cole-Cole

parameter with the widest interval range and is often the most poorly resolved parameter, which gives rise to the only moderately resolved layer thickness.

Field example

To show the influence of TDIP data in an analysis of field measurements, two 1D vertical soundings (two meters apart) are extracted from a larger 2D profile acquired in Grindsted, Denmark, and inverted together. The local geology is dominated by 60 m of Miocene sands, but a borehole drilled close to the soundings identifies a thin layer of clay and sandy clay (thickness ~ 2 m) close to the surface (depth ~ 1.5 m). To focus on this low-resistivity clay layer, only the top 15 meters of the soundings are considered.

The applied data were acquired with 12 different electrode configurations, where the IP decays are measured between 3.5-4000 ms with a 100% duty cycle with the Terrameter LS instrument (ABEM instruments AB). The IP decays were extracted from the raw full-waveform recordings, sampled at 3750 Hz, using the algorithm described in Olsson et al. (2016).

The measured data are shown in Figure 6. The DC data are inverted with the MCMC algorithm and then compared to the MCMC inversion results of the combined DCIP data (Figure 7). For the DC inversion, the results show strong equivalences and undetermined parameters (Figure 7, Panel-DC). The STDFs computed from the MCMC inversion results are presented in Table 4. Both the resistivity and the thickness of the clay layer determined by the DC inversion are unresolved (Table 4, Row 1). However, as for a classic low-resistivity equivalence problem, the conductance is resolved. Besides the equivalence problem, this poor resolution may also be due to the limited number of DC data points in

the top two layers (Figure 6). However, for the DCIP inversion the low-resistivity layer is well-resolved (Table 4, Row 2) and fits the borehole information (Figure 7, Panel-DCIP). This means that the information given in the IP signals resolves the thickness-resistivity equivalences.

The results of the linearized inversion of the field data, i.e. the linearized inversion applied to determine the start model for the MCMC analysis (Table 2, Step 2), are also shown in Figure 7 (blue line) and the linearized uncertainty analysis is listed in Table 4 (Row 3-4). The linearized inversion of DC data finds the low resistivity layer, but the thickness and the resistivity of the layer is unresolved and so is the conductance. The linearized inversion of the DCIP data agrees well with the MCMC inversion results for the resistivity and thickness of the layer. For this field example, the STDFs in Table 4 show that the linearized analysis underestimates the resolution of the parameters compared to the MCMC approach.

DISCUSSION

In this study, we have used the MCMC inversion approach as a tool to invert TD DCIP data in order to study equivalent models and obtain a non-linearized sensitives analysis of the model parameters. We do not, however, suggest the MCMC approach as a general scheme for inversion of 2D and 3D datasets as the computation time would be immense (at least for full-decay modelling). Despite the time reduction gained by applying the posterior covariance for scaling the sampling algorithm, the time required to invert a 2D dataset is still days with the MCMC scheme compared to up to a few hours for the linearized approach. That said, the MCMC approach still has its advantages over gradient-based linearized methods when it comes to quantifying model parameter uncertainties and

correlations. In difference to gradient-based methods where the inversion result is one "best fitting" model, it is possible with the MCMC approach to study the space of models that all fit the observed data to a certain degree. Furthermore, it was found that the MCMC approach is largely independent on the start model of the inversion, which is not always the case for gradient-based inversions.

In this study, we have chosen to focus on time-domain DCIP data. However, the same results are expected for frequency-domain data as preliminary MCMC studies have shown that the sensitivity of the Cole-Cole parameters retrieved from time-domain or frequency-domain are comparable.

CONCLUSION

By inverting synthetic DC resistivity data with a Metropolis-Hastings MCMC algorithm, we have studied well-known resistivity-thickness equivalences present in DC inversion results. We have then combined DC data with full-waveform time-domain induced polarization (TDIP) data and found that the TDIP data help to resolve the layer thicknesses and thereby the resistivities in models with low-resistivity and high-resistivity equivalence problems. This is possible because no major thickness equivalences are present for the IP parameters. The results show that the increase in resolution depends on the added chargeability contrast between the layers (modelled in term of the Cole-Cole IP parameters) as well as the settings causing the equivalence, i.e. the layer thicknesses and the resistivity contrasts in the model. In the models studied, it was found that a contrast of a factor of six in the chargeability (which can easily be expected in the field, e.g. if a clay layer is embedded in a sand formation) is enough the resolve strong equivalences. Furthermore, inversion of a DCIP field data set shows that a thin clay layer embedded in a sand

formation causes strong equivalences and ambiguities in the retrieved models when only considering the DC data. However, when the IP data are added to the inversion, the clay layer is resolved. This was found to be the case for both a MCMC and a linearized inversion approach.

Combined, the results indicate that equivalent layer sequences can be resolved by adding IP data to the inversion. Considering that time-domain IP data can be collected by most instruments when collecting DC resistivity data, the DC equivalence problems can be significantly reduced at very little additional cost.

ACKNOWLAGEMENT

This work was supported by the project GEOCON (Advancing GEOlogical, geophysical and CONtaminant monitoring technologies for contaminated site investigation, www.geocon.env.dtu.dk).

REFERENCES

Aristodemou, E. and Thomas-Betts, A., 2000, DC resistivity and induced polarisation investigations at a waste disposal site and its environments: Journal of Applied Geophysics, **44,** 275-302.

Auken, E., Christiansen, A. V., Jacobsen, B. H., Foged, N. and Sørensen, K. I., 2005, Piecewise 1D Laterally Constrained Inversion of resistivity data: Geophysical Prospecting, **53,** 497-506.

Binley, A. and Kemna, A. 2005. DC resistivity and induced polarization methods. Springer.

Chongo, M., Christiansen, A. V., Fiandaca, G., Nyambe, I. A., Larsen, F. and Bauer-Gottwein, P., 2015, Mapping localised freshwater anomalies in the brackish paleo-lake sediments of the Machile-Zambezi Basin with transient electromagnetic sounding, geoelectrical imaging and induced polarisation: Journal of Applied Geophysics, **2015,** 81-92.

Christiansen, A. V., Auken, E., Foged, N. and Sørensen, K. I., 2007, Mutually and laterally constrained inversion of CVES and TEM data - A case study: Near Surface Geophysics, **5,** 115-124.

Cole, K. S. and Cole, R. H., 1941, Dispersion and absorption in dielectrics: Journal of Chemical Physics, **9,** 341-351.

Fiandaca, G., Auken, E., Gazoty, A. and Christiansen, A. V., 2012, Time-domain induced polarization: Full-decay forward modeling and 1D laterally constrained inversion of Cole-Cole parameters: Geophysics, **77,** E213-E225.

Fiandaca, G., Ramm, J., Binley, A., Gazoty, A., Christiansen, A. V. and Auken, E., 2013, Resolving spectral information from time domain induced polarization data through 2-D inversion: Geophysical Journal International, **192,** 631-646.

Fitterman, D. V., Meekes, J. a. C. and Ritsema, I. L., 1988, Equivalence behavior of three electrical sounding methods as applied to hydrogeological problems, in: 50th Annual EAGE, The Hauge.

Gazoty, A., Fiandaca, G., Pedersen, J., Auken, E. and Christiansen, A. V., 2012a, Mapping of landfills using time-domain spectral induced polarization data: The Eskelund case study: Near Surface Geophysics, **10,** 575-586.

Gazoty, A., Fiandaca, G., Pedersen, J., Auken, E., Christiansen, A. V. and Pedersen, J. K., 2012b, Application of time domain induced polarization to the mapping of lithotypes in a landfill site: Hydrol. Earth Syst. Sci., **16,** 1793-1804.

Gazoty, A., Fiandaca, G., Pedersen, J., Auken, E. and Christiansen, A. V., 2013, Data repeatability and acquisition techniques for Time-Domain spectral Induced Polarization: Near Surface Geophysics, **11,** 391-406.

Hastings, W. K., 1970, Monte Carlo sampling methods using Markov chains and their applications: Biometrika, **57,** 97-109.

Hönig, M. and Tezkan, B., 2007, 1D and 2D Cole-Cole-inversion of time-domain induced-polarization data: Geophysical Prospecting, **55,** 117-133.

Johansson, S., Fiandaca, G. and Dahlin, T., 2015, Influence of non-aqueous phase liquid configuration on induced polarization parameters: Conceptual models applied to a time-domain field case study: Journal of Applied Geophysics, **123,** 295-309.

Johansson, S., Sparrenbom, C., Fiandaca, G., Lindskog, A., Olsson, P.-I., Dahlin, T. and Rosqvist, H., 2016, Investigations of a Cretaceous limestone with spectral induced polarization and scanning electron microscopy: Geophysical Journal International**,** ggw432.

Knödel, K., Lange, G. and Voigt, H.-J., 2007. Environmental geology: Handbook of field methods and case studies, Springer Science & Business Media.

Koefoed, O., 1979. Geosounding principles, 1. Resistivity Sounding Measurements, Elsevier.

Leroux, V., Dahlin, T. and Svensson, M., 2007, Dense resistivity and induced polarization profiling for a landfill restoration project at Härlöv, Southern Sweden: Waste Management & Research, **25,** 49-60.

Madsen, L. M., Kirkegaard, C., Fiandaca, G., Christiansen, A. V. and Auken, E., 2016, An analysis of Cole-Cole parameters for IP data using Markov chain Monte Carlo. IP2016/4th International Workshop on Induced Polarization, Aarhus, Denmark, Available at: http://hgg.au.dk/2017-inaktive-sider/ip2016/abstracts-presentations-posters/, accesed 11 October 2017

Maurya, P. K., Fiandaca, G., Auken, E. and Christiansen, A. V., 2016, Lithological characterization of a comtaminated site using direct current resistivity and time domain induced polarization. IP2016/4th International Workshop on Induced Polarization, Aarhus, Denmark, Available at: http://hgg.au.dk/2017-inaktive-sider/ip2016/abstracts-presentations-posters/, accesed 11 October 2017

Metropolis, N., Rosenbluth, A. W., Rosenbluth, M. N., Teller, A. H. and Teller, E., 1953, Equation of state calculations by fast computing machines: The journal of chemical physics, **21,** 1087-1092.

Mosegaard, K. and Tarantola, A., 1995, Monte Carlo sampling of solutions to inverse problems: Journal of Geophysical Research: Solid Earth, **100,** 12431-12447.

Mosegaard, K. and Tarantola, A. 2002. Probabilistic Approach to Inverse Problems. In: Lee, W., Kisslingers, C., and Kanamori, H., International handbook of earthquake and engineering seismology: Academic Press.

Olsson, P. I., Dahlin, T., Fiandaca, G. and Auken, E., 2015, Measuring time-domain spectral induced polarization in the on-time:decreasing acquisition time and increasing signal-to-noise ratio: Journal of Applied Geophysics, **123,** 316-321.

Olsson, P. I., Fiandaca, G., Larsen, J. J., Dahlin, T. and Auken, E., 2016, Doubling the spectrum of time-domain induced polarization by harmonic de-noising, drift correction, spike removal, tapered gating, and data uncertainty estimation: Geophysical Journal International, **207 (2),** 774-784.

Pelton, W. H., Ward, S. H., Hallof, P. G., Sill, W. R. and Nelson, P. H., 1978, Mineral discrimination and removal of inductive coupling with multifrequency IP: Geophysics, **43,** 588-609.

Raiche, A. P., Jupp, D. L. B., Rutter, H. and Vozoff, K., 1985, The joint use of coincident loop transient electromagnetic and Schlumberger sounding to resolve layered structures: Geophysics, **50,** 1618-1627.

Sandberg, S. K., 1993, Examples of resolution improvement in geoelectrical soundings appplied to groundwater investigations: Geophysical Prospecting, **41,** 207-227.

Seara, J. L. and Granda, A., 1987, Interpretation of I.P. time domain/resistivity soundings for delineating sea-water intrusions in some coastal areas of the northeast of Spain: Geoexploration, **24,** 153-167.

Sogade, J. A., Scira-Scappuzzo, F., Vichabian, Y., Shi, W., Rodi, W., Lesmes, D. P. and Morgan, F. D., 2006, Induced-polarization detection and mapping of contaminant plumes: Geophysics, **71,** B75-B84.

Tarantola, A., 2005. Inverse Problem Theory and Methods for Model Parameter Estimation, Siam.

Tarantola, A. and Valette, B., 1982a, Generalized nonlinear inverse problems solved using a least squares criterion: Reviews of Geophysics and Space Physics, **20,** 219-232.

Tarantola, A. and Valette, B., 1982b, Inverse problems = quest for information: J. of Geophysics, **50,** 159-170.

Vozoff, K. and Jupp, D. L. B., 1975, Joint inversion of geophysical data: Geophysical Journal Of The Royal Astronomical Society, **42,** 977-991.

FIGURE AND FIGURE CAPTION

Figure 1:

The apparent resistivity forward response and associated error bars computed from a three-layer model with the parameter values: thk = [10, 5] m and ρ = [200, 20, 200] Ωm. The apparent resistivity, ρ_a, is plotted against a pseudo depth. The error bars correspond to two standard deviations.

Figure 2:

Panel-DC) MCMC inversion results of a model with the resistivity values ρ = [200, 20, 200] Ωm. The middle layer has a low-resistivity equivalence, where the thickness and the resistivity are strongly correlated and unresolved. The black lines are models accepted by the MCMC algorithm, and the density of the lines illustrates the posterior probability density. The dashed yellow line shows the model, which has the highest probability. Panel-DCIP) MCMC inversion result of synthetic DCIP data generated from the model: ρ = [200, 20, 200] Ωm, m_0 = [20, 200, 20] mV/V, τ = 1 s, and c = 0.6.

Figure 3:

Forward response of the IP model given in Figure 2 (Panel DCIP). Each line illustrates the data measured in one of the 35 time gates with the earliest time gate at the top of the plot (every second time gate is shown here). Examples of the two standard deviation error bars are shown for three of the time gates (black lines).

Figure 4:

Panel-DC) MCMC inversion results of a model with the resistivity values ρ = [20, 200, 20] Ωm. Panel-DCIP) MCMC inversion result of synthetic DCIP data generated from the model: ρ = [20, 200, 20] Ωm, m_0 = [20, 200, 20] mV/V, τ = 1 s, and c = 0.6.

Figure 5:

Standard deviation factors (STDFs) of the thickness of the second layer, *thk*(2), in a three-layer model. The STDFs are plotted against the contrast in the Cole-Cole parameter between the layers. The default three-layer model has the same Cole-Cole parameters in all three layers: ρ = 200 Ωm, m_0 = 100 mV/V, τ = 1 s, and c = 0.6. The thickness of the top and second layer are 10 m and 5 m, respectively. A parameter contrast between the layers is then obtained by changing the value of one of the parameters in the second layer. As an example, the STDF of *thk*(2) is 1.5 for a factor three contrast in the τ (i.e. ρ = 200 Ωm, m^0 = 100 mV/V, τ = [1,3,1] s, and c = 0.6). Note: If the STDF of a parameter is above 2.5, i.e. completely unresolved, the STDF is put to 2.5 in the figure.

Figure 6:

DC data (a) and IP data (b) with error bars (two standard deviations) from two vertical soundings (red and blue curves) measured in Grindsted, Denmark. For the IP data (b), each curve represents a time gate of the measured IP decays. Only four of 29 time gates are shown here.

Figure 7:

DC and DCIP inversion results of field data from Grindsted, Denmark. The black lines are models accepted to the posterior probability distribution by the MCMC algorithm, the yellow dashed line is the model at the maximum of the distribution, and the blue line is the model found by a linearized inversion approach. The brown vertical lines mark the top and bottom of a clay layer and a sandy clay layer.

Table 1:

Electrode configuration of the 20 quadrupoles applied for generating synthetic vertical soundings.

Table 2:

Metropolis-Hastings algorithm applied for inversion of DC and DCIP data.

Table 3:

Standard deviation factors (STDFs) of the models parameters, resistivity and thickness, of a three-layer model (Figure 2) determined from a MCMC inversion of DC and DCIP data, respectively. Non-values indicate unresolved parameters.

Table 4:

Standard deviation factors (STDFs) computed from inversion results of DC and DCIP field data. For the MCMC approach, the STDFs are computed from the mean of the posterior probability distributions. For the linearized inversion approach, the STDFs are computed from the linearized estimated covariance matrix (Eq. 6). Non-values indicate unresolved parameters.

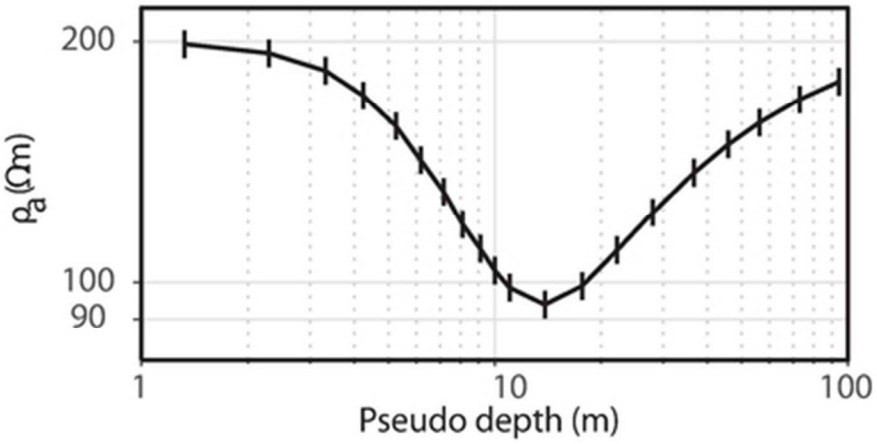

The apparent resistivity forward response and associated error bars computed from a three-layer model with the parameter values: *thk* = [10, 5] m and ρ = [200, 20, 200] Ωm. The apparent resistivity, ρ_a, is plotted against a pseudo depth. The error bars correspond to two standard deviations.

38x19mm (300 x 300 DPI)

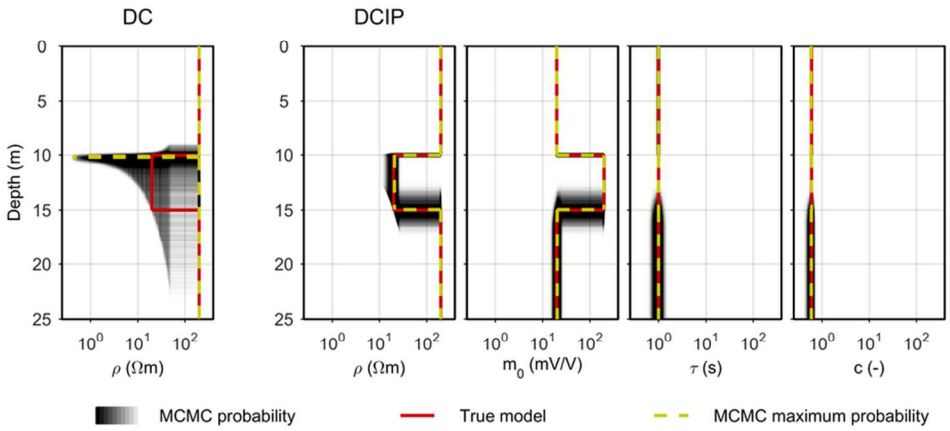

Panel-DC) MCMC inversion results of a model with the resistivity values ρ = [200, 20, 200] Ωm. The middle layer has a low-resistivity equivalence, where the thickness and the resistivity are strongly correlated and unresolved. The black lines are models accepted by the MCMC algorithm, and the density of the lines illustrates the posterior probability density. The dashed yellow line shows the model, which has the highest probability. Panel-DCIP) MCMC inversion result of synthetic DCIP data generated from the model: ρ = [200, 20, 200] Ωm, m_0 = [20, 200, 20] mV/V, τ = 1 s, and c = 0.6.

82x41mm (300 x 300 DPI)

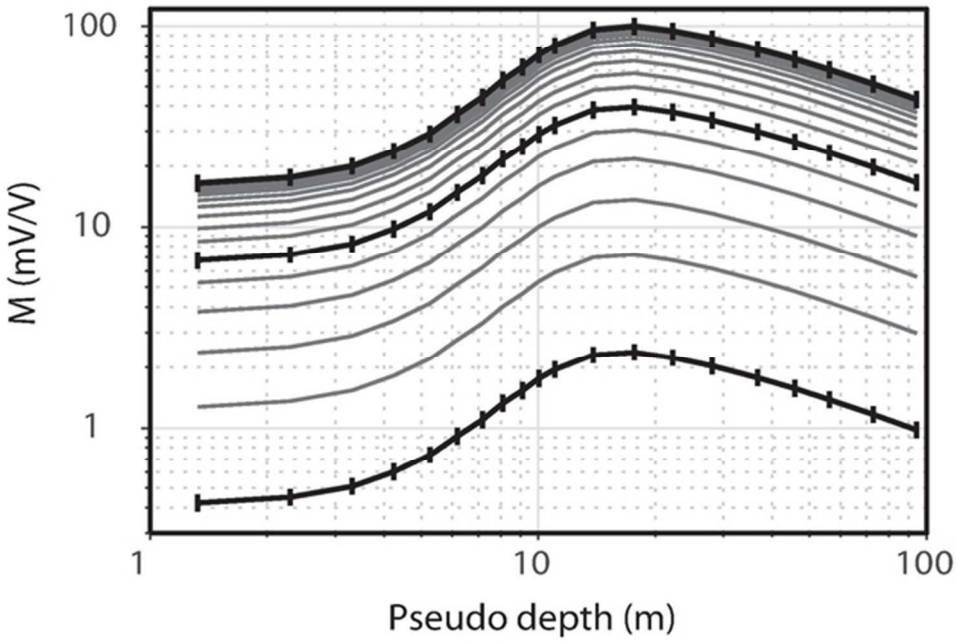

Forward response of the IP model given in Figure 2 (Panel DCIP). Each line illustrates the data measured in one of the 35 time gates with the earliest time gate at the top of the plot (every second time gate is shown here). Examples of the two standard deviation error bars are shown for three of the time gates (black lines).

55x40mm (300 x 300 DPI)

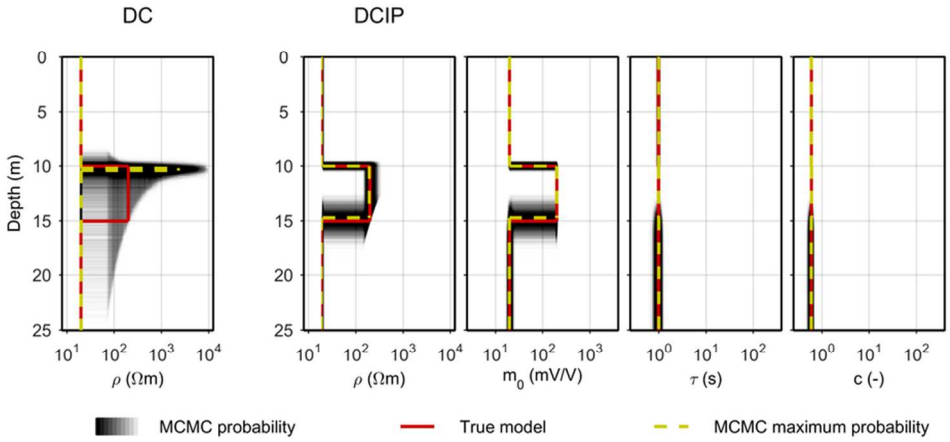

Panel-DC) MCMC inversion results of a model with the resistivity values ρ = [20, 200, 20] Ωm. Panel-DCIP) MCMC inversion result of synthetic DCIP data generated from the model: ρ = [20, 200, 20] Ωm, m_0 = [20, 200, 20] mV/V, τ = 1 s, and c = 0.6.

82x41mm (300 x 300 DPI)

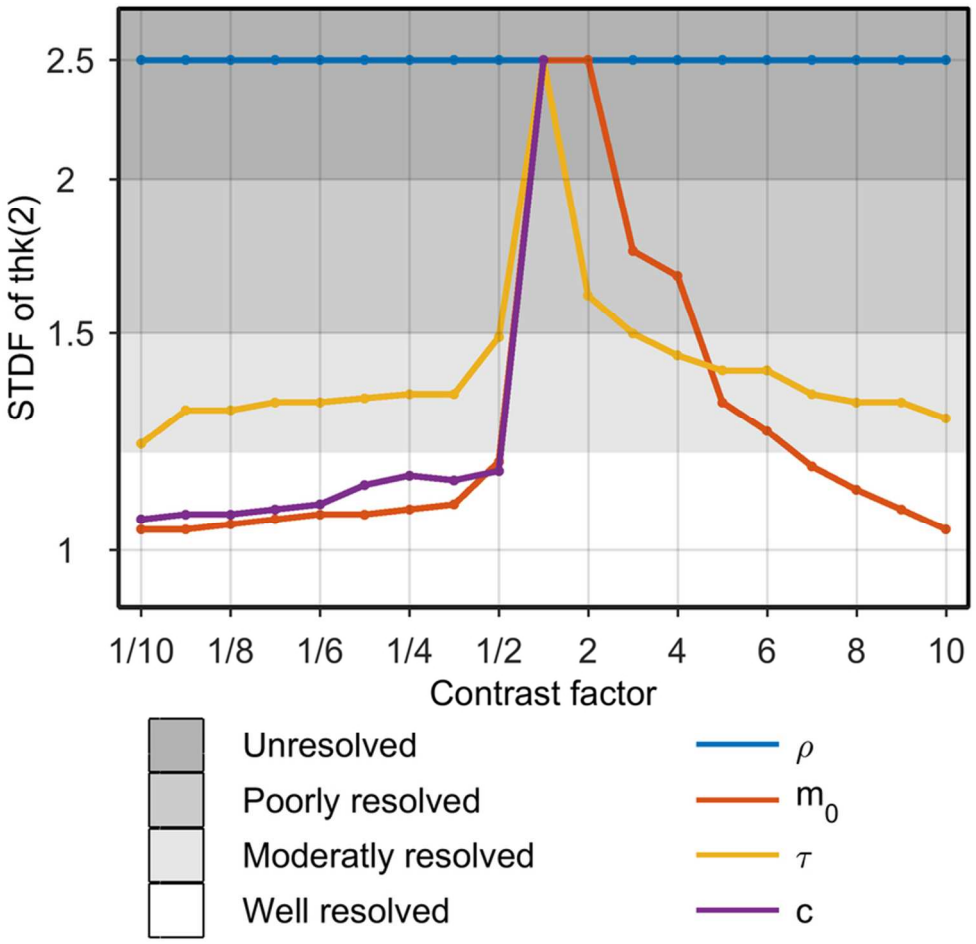

Standard deviation factors (STDFs) of the thickness of the second layer, *thk*(2), in a three-layer model. The STDFs are plotted against the contrast in the Cole-Cole parameter between the layers. The default three-layer model has the same Cole-Cole parameters in all three layers: ρ = 200 Ωm, m_0 = 100 mV/V, τ = 1 s, and c = 0.6. The thickness of the top and second layer are 10 m and 5 m, respectively. A parameter contrast between the layers is then obtained by changing the value of one of the parameters in the second layer. As an example, the STDF of *thk*(2) is 1.5 for a factor three contrast in the τ (i.e. ρ = 200 Ωm, m^0 = 100 mV/V, τ = [1,3,1] s, and c = 0.6). Note: If the STDF of a parameter is above 2.5, i.e. completely unresolved, the STDF is put to 2.5 in the figure.

77x73mm (300 x 300 DPI)

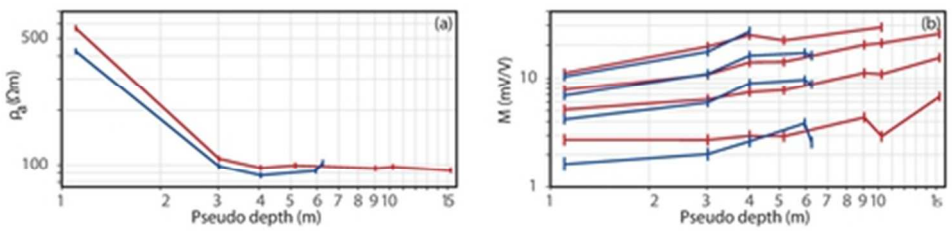

DC data (a) and IP data (b) with error bars (two standard deviations) from two vertical soundings (red and blue curves) measured in Grindsted, Denmark. For the IP data (b), each curve represents a time gate of the measured IP decays. Only four of 29 time gates are shown here.

42x10mm (300 x 300 DPI)

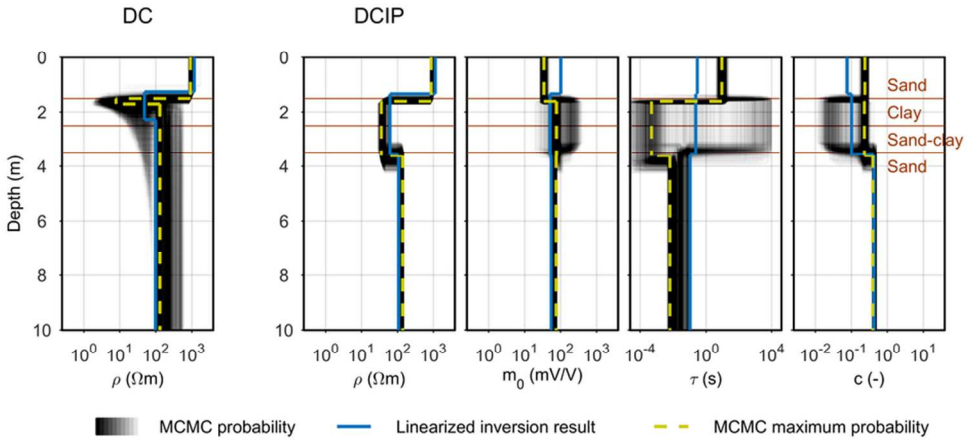

DC and DCIP inversion results of field data from Grindsted, Denmark. The black lines are models accepted to the posterior probability distribution by the MCMC algorithm, the yellow dashed line is the model at the maximum of the distribution, and the blue line is the model found by a linearized inversion approach. The brown vertical lines mark the top and bottom of a clay layer and a sandy clay layer.

82x41mm (300 x 300 DPI)

Table 1: Electrode configuration of the 20 quadrupoles applied for generating synthetic vertical soundings.

Quadrupole	**1**	**2**	**3**	**4**	**5**	**6**	**7**	**8**	**9**	**10**
|AB| (m)	7.5	12.5	17.5	22.5	27.5	32.5	37.5	42.5	47.5	52.5
|MN| (m)	2.5	2.5	2.5	2.5	2.5	2.5	2.5	2.5	2.5	2.5
Quadrupole	**11**	**12**	**13**	**14**	**15**	**16**	**17**	**18**	**19**	**20**
|AB| (m)	57.5	72.5	92.5	117.5	147.5	192.5	240	305	390	500
|MN| (m)	2.5	2.5	2.5	15	15	15	15	65	65	65

Table 2: Metropolis-Hastings algorithm applied for inversion of DC and DCIP data.

1: Set N_{ite}, k_{step}

2: Run linearized inversion to determine start model, $\mathbf{m_{start}}$, and the covariance matrix, $\boldsymbol{C_{est}(m_{start})}$

3: $\mathbf{m_{cur}} = \mathbf{m_{start}}$

4: **for** $i = 1, N_{ite}$ **do**

5: Compute a new model proposal:

$$\boldsymbol{m_{new}} = \boldsymbol{m_{cur}} + \boldsymbol{L}\,\boldsymbol{n}\,k_{step}$$

6: Compute acceptance probability

$$P_{acc} = \frac{P_{like}(\boldsymbol{m_{new}})}{P_{like}(\boldsymbol{m_{cur}})}$$

7: Draw random number (α) from a uniform distribution [0:1]

8: **if** $P_{acc} > \alpha$

9: $\mathbf{m_{cur}} = \mathbf{m_{new}}$

10: **else**

11: $\mathbf{m_{cur}} = \mathbf{m_{cur}}$

12: **end if**

13: **end for**

Table 3: Standard deviation factors (STDFs) of the models parameters, resistivity and thickness, of a three-layer model (Figure 2) determined from a MCMC inversion of DC and DCIP data, respectively. Non-values indicate unresolved parameters.

	$\boldsymbol{STDF(\rho_1)}$	$\boldsymbol{STDF(\rho_2)}$	$\boldsymbol{STDF(\rho_3)}$	$\boldsymbol{STDF(thk_1)}$	$\boldsymbol{STDF(thk_2)}$
DC	1.01	-	1.02	1.03	-
DCIP	1.01	1.17	1.02	1.01	1.2

Table 4: Standard deviation factors (STDFs) computed from inversion results of DC and DCIP field data. For the MCMC approach, the STDFs are computed from the mean of the posterior probability distributions. For the linearized inversion approach, the STDFs are computed from the linearized estimated covariance matrix (Eq. 6). Non-values indicate unresolved parameters.

Type	**STDF(ρ_2)**	**STDF(thk_2)**	**STDF(ρ_2/thk_2)**
MCMC - DC	-	-	1.2
MCMC - DCIP	1.14	1.11	1.17
Linearized - DC	-	-	-
Linearized - DCIP	1.3	1.5	1.5